Analytical calculation and observation of the magnetic contrast in magneto-optical studies of magnetic cylinders

K. Richter,[1,2] A. Thiaville,[1] and R. Varga[2]

[1]*Laboratoire de Physique des Solides, Université Paris-Sud, CNRS UMR 8502, 91405 Orsay, France*

[2]*Department of Physics, Pavol Jozef Safarik University, 04154 Kosice, Slovakia*

(Received 21 February 2017; revised manuscript received 18 May 2017; published 17 August 2017)

The nonplanar sample surface is a crucial feature that must be taken into account for a good interpretation of magneto-optical observations of magnetic cylindrical microwires. This is due to the fact that a curved topography gives rise to a spatial distribution of local planes of incidence as a function of position on the circumference of a cylinder. Analytical calculations of the magnetic contrast of magnetic cylinders spontaneously magnetized in the axial direction reveal that an axial magnetization reversal produces a characteristic black-and-white magneto-optical contrast and that it does not correspond to two oppositely magnetized domains, as would be concluded in the case of planar samples. Optical and magneto-optical observations of thin cylindrical FeSiB wires support this model. Calculations are also performed for the cases of circular and polar magnetizations.

DOI: 10.1103/PhysRevB.96.064421

I. INTRODUCTION

A reliable determination of the surface magnetization on samples with curved topography is necessary for proposed spintronic devices utilizing three-dimensional structures [1] that are supposed to substitute current laterally patterned nanomagnets [2,3]. While several experimental techniques allow for very controllable deposition of magnetic structures with complex geometries at the nano- and microscales [4], a reliable characterization of the surface magnetization by conventional experimental techniques usually meets several obstacles in the case of samples with a curved surface. The magneto-optical Kerr effect (MOKE) is widely employed in research and industrial applications to study the surface magnetization of materials since in a first-order approximation the MOKE signal is proportional to the magnetization of the studied material. While MOKE is widely used to investigate surface magnetism of planar samples like thin multilayered films [5] or planar nanowires [6], it was only recently demonstrated that the curved topography of samples is responsible for peculiar magneto-optical contrasts, which cannot be explained well within the simple planar surface approximation [7,8]. The thorough understanding of these contrasts is particularly important as domain walls in cylindrical ferromagnets are predicted to be massless objects and potentially break the Walker limit [9]. Extremely fast domain wall propagation has been reported [10,11] in thin magnetic cylinders with a diameter of 10–100 μm. It was shown that fast domain wall motion in this material can be tuned by mechanical stress [12,13], temperature [14,15], or perpendicular field [16] even though the exact spin structure of the domain wall in the material is not clear. It is evident that a key prerequisite for understanding the fast reversal is detailed knowledge of surface magnetization processes. Several optical and magneto-optical studies have been devoted to nonplanar samples like corrugated surfaces [17] and thin cylindrical wires with negative magnetostriction [18–22], in which a typical bamboo domain structure was found. However, most such studies so far have been based on the assumption that the cylindrical shape of the wire can be neglected, approximating it by a planar sample.

In this paper, we perform an analytical calculation of the magneto-optic contrast of ferromagnetic cylinders. The calculation is carried out within a physical-optics approximation for cylinders with a large diameter (compared to the wavelength of light), where diffraction effects can be neglected. It is shown that the curvature of the sample surface is a crucial factor that must be taken into account in the interpretation of magneto-optical observations of thin cylinders. This paper is organized in the following manner. First, the role of topography is examined for reflection of linearly polarized light from a cylindrical surface. Within the physical-optics approximation, it is recalled that the cylindrical shape of wires gives rise to a spatially dependent orientation of the local planes of incidence. If the cylinder is observed along its main axis by linearly polarized light, the polarization of each ray can be decomposed into two components of local polarization oriented perpendicular and parallel to the local plane of incidence. Since both of these local polarization components experience different reflection coefficients, the polarization of the reflected ray is changed, which, in turn, gives rise to a characteristic light intensity profile consisting of two light stripes when observed by a microscope with a crossed polarizer and analyzer. In the second part, a full analytic calculation of magneto-optical contrast for the spontaneously magnetized cylinder with axial, circular, and polar magnetizations is presented. It is shown that each of these surface magnetization directions gives a characteristic magneto-optical contrast. While the axial change of the surface magnetization produces in MOKE microscopy two black and white stripes oriented along the main axis of the cylinder, in the case of circular magnetization, the two stripes of magnetic contrast are of the same polarity. Our theoretical results are compared to experimental observations. The magneto-optics of cylinders is a first step towards the generalization of MOKE microscopy to nonplanar samples in the optical range with more complex geometries.

II. EXPERIMENT

The magneto-optical observations are performed on cylindrical wires produced with the Taylor-Ulitovski method [23].

This fabrication process involving drawing and rapid quenching ensures a cylindrical sample shape [24] with a well-defined diameter of the metallic core, which is desirable for the study. In our case, a 2-cm-long $Fe_{77.5}Si_{7.5}B_{15}$ sample has been used for the observations. This composition is characterized by a high iron content, which gives rise to a strong magneto-optical effect [25]. The sample had a total diameter (metallic core plus glass thickness) of 33 μm, with a metallic core diameter of 15 μm. Microwires of such diameter and glass thickness have been studied previously [26] because of their observed high domain wall velocities.

The magneto-optical observation was carried out on a commercial EVICO Imager.D2m Zeiss polarizing microscope [22]. The microscope uses Köhler illumination that gives separate access to the back focal plane and the object plane. The direction of the incident light beam can be varied by the position of an aperture diaphragm relative to optical axis, which allows us to set up all configurations of MOKE.

The maximum angle of incidence was increased by use of Zeiss 518C immersion oil that was applied between the objective and sample. The refraction index of immersion oil ($n_{\mathrm{oil}} = 1.518$ at 23 °C) is very close to that of glass, which helps remove parasitic optical effects of the glass coating (like multiple internal reflections or reflectivity at the air-glass interface). Images were captured by a high-resolution Hamamatsu ORCA-03G digital camera.

III. RESULTS: PHYSICAL-OPTICS CALCULATIONS AND COMPARISON TO EXPERIMENTS

In MOKE microscopy, the magnetic contrast is based on the change in light intensity that stems from interaction of linearly polarized light with surface magnetization. Thus, we start in this section with basic geometric calculations revealing the interplay between linear polarization of light and reflection from a cylindrical sample (optics), which will be used to evaluate magneto-optical effects. As noted above, the calculation is carried out for cylindrical microwires, so that diffraction effects can be neglected, and the physical optics approximation is justified. Although this physics is well known (see [27], for example), the magnetic case is less known, and the magnetic cylinder geometry has not been treated, so we quickly derive the necessary formulas.

A. Role of the cylindrical geometry of sample

Let x be the axis of the cylinder and z be the vertical direction. If the cylinder is illuminated along its main axis by an incident light beam consisting of parallel rays (e.g., a laser beam), the optical geometry can be described by two parameters in a cylindrical coordinate system. The first is the radial angle θ, which defines the position on the cylinder's surface (Fig. 1) by the local normal $\vec{n}$:

$$\vec{n} = \begin{pmatrix} 0 \\ \sin\theta \\ \cos\theta \end{pmatrix}. \tag{1}$$

This vector is vertical at the cylinder top ($\theta = 0$) and horizontal for $\theta = \pi/2$ (Fig. 1, right). The second parameter is the global angle of incidence I, formed between the normal at the cylinder's top and the direction of the incident beam. It defines the vector of incidence $\vec{I}$:

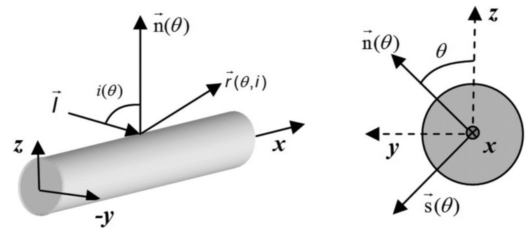

FIG. 1. Schematic of the main parameters used: $\vec{I}$ is the direction of the incident beam with global angle of incidence I, θ is the circumferential angle defining a position on the cylinder surface, $\vec{n}$ is the local normal to the cylinder, $i(\theta)$ is the local angle of incidence, and $\vec{r}$ is the direction of the local reflected ray.

$$\vec{I} = \begin{pmatrix} \sin I \\ 0 \\ -\cos I \end{pmatrix}, \tag{2}$$

which is constant for all rays of the incident beam (Fig. 1).

In accord with the law of reflection, the emerging rays have a direction given by the vector $\vec{r}$:

$$\vec{r}(\theta, I) = \begin{pmatrix} \sin I \\ \sin 2\theta \cos I \\ \cos 2\theta \cos I \end{pmatrix}. \tag{3}$$

In contrast to the incident beam, the direction of the reflected rays is a function of both the global angle of incidence I and the radial angle θ. It means that for any given value of the global angle of incidence, the direction of the reflected ray depends on the circumferential position on the cylindrical surface. Even though the sample is illuminated by a beam consisting of parallel rays, they are no longer parallel after reflection from the cylindrical surface but form a diverging beam that appears in experiment as an asymmetric light cone with an elliptical base, whose main axis is along z (Fig. 1). Such a divergence of the reflected rays is a direct consequence of the nonplanar shape of the cylindrical surface.

As seen from Eqs. (1) and (2), the local angle of incidence $i(\theta)$ changes with the circumferential angle θ according to

$$\begin{aligned} \cos[i(\theta)] &= -\vec{I}\cdot\vec{n} = \cos I\ \cos\theta, \\ \sin[i(\theta)] &= \sqrt{1-\cos^2 I \cos^2\theta} = \sqrt{\sin^2\theta + \sin^2 I \cos^2\theta} \\ &= \sqrt{\sin^2 I + \sin^2\theta \cos^2 I}. \end{aligned} \tag{4}$$

Figure 2 plots the circumferential dependence of the local angle of incidence for different global angles of incidence. Independent of the value of the global angle of incidence, the minimum local angle of incidence is always achieved at the top of cylinder ($\theta = 0°$), where the local angle of incidence is equal to the global angle of incidence. As the θ angle increases, the angle of incidence becomes bigger than the global angle of incidence and reaches its maximum of 90° at $\theta = 90°$, independent of the value of the global angle of incidence I. This variation of the angle of incidence will be shown to be important for the resulting magneto-optical contrast.

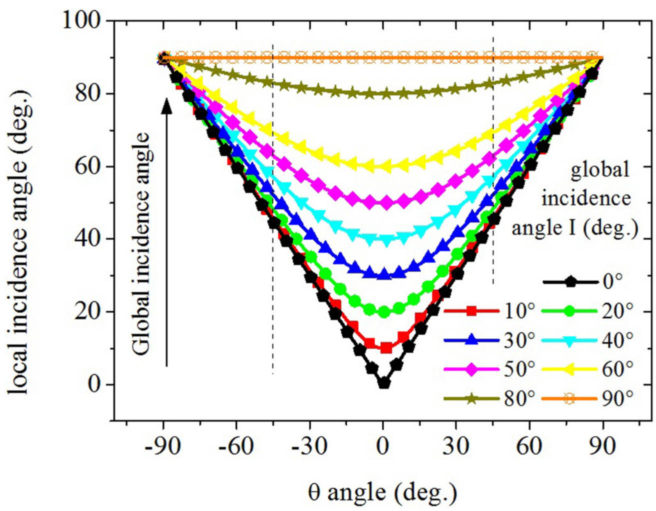

FIG. 2. Calculated local angle of incidence as a function of circumferential position on the cylinder surface given by the angle θ for different values of the global angle of incidence I. Dashed vertical lines depict the maximum angle ($\pm 45^\circ$) that can be observed in the microscope.

The circumferential dependence of the angle of incidence that can be observed is limited by the numerical aperture of the objective. Defining a local numerical aperture na $[\theta, I]$ as the sine of the angle between the vertical and the locally reflected ray, we obtain from Eq. (3)

$$\mathrm{na}\,[\theta, I] = \sqrt{\sin^2 I + \sin^2 2\theta\, \cos^2 I}. \tag{5}$$

Figure 3 shows how the local numerical aperture depends on its two variables. The shape of the curve can be explained by the variation of the z component of the reflectance vector, Eq. (3).

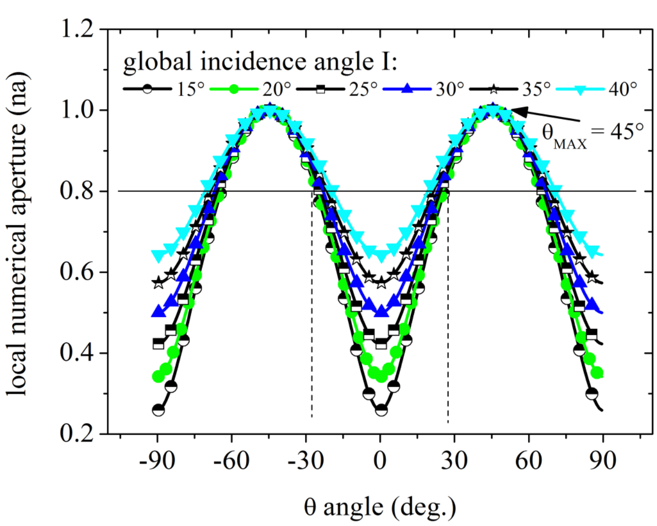

FIG. 3. Calculated local numerical aperture as a function of angle θ. Independent of the value of the global angle of incidence I, the local numerical aperture reaches a maximum value (1) at $\theta = 45^\circ$. At this angle, rays are reflected into the xy horizontal plane. The numerical aperture of the objective lens is depicted by a horizontal thin line and sets the maximum interval of the microwire surface ($-30^\circ < \theta < 30^\circ$) that can be observed with this objective lens.

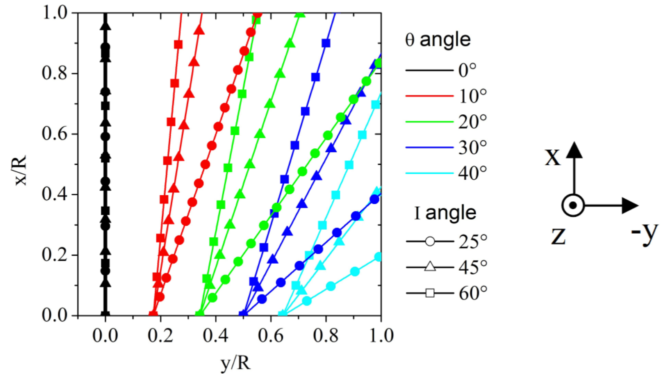

FIG. 4. Reflection from a cylindrical surface causing an inclination of the planes of incidence. For each position on the cylinder surface (angle θ), the y abscissa at $x = 0$ is the vertical projection of this point on the top xy plane, i.e.,$y/R(x = 0) = \sin\theta$, in order to separate the various families of lines.

For $\theta < 45^\circ$, this component is always positive, which means that the reflected ray points towards the upper half-space of the incident rays. Increasing the angle θ leads to a progressive tilting of the reflected ray towards the xy plane, which is fully achieved at $\theta = 45^\circ$. The numerical aperture reaches its maximum at this angle, independent of the global angle of incidence I (Fig. 3). For $\theta > 45^\circ$ and $\theta < -45^\circ$, the rays are reflected below the xy plane (towards the $-z$ axis). Therefore, only the surface of the cylinder with $-45^\circ < \theta < 45^\circ$ can be observed by optical microscopy, even if an objective of maximum numerical aperture is used.

In addition to the varying angle of incidence and numerical aperture, the cylindrical shape of the surface affects the geometry of the planes of incidence as well. Due to the θ dependence of the normal, Eq. (1), the planes of incidence are not parallel to each other but show an inclination with respect to the wire axis. Figure 4 draws the lines formed by the intersection of the planes of incidence with the horizontal plane. A simple calculation from Eqs. (1) and (2) shows that the inclination angle α of the lines with respect to the x axis obeys $\tan\alpha = \tan\theta / \tan I$.

The spatially dependent orientation of the planes of incidence has an important impact on optical magnetometric measurements, where a linearly polarized light with a crossed analyzer is used. Even though the cylinder is illuminated by a global "s" or "p" linearly polarized light (with respect to the plane of incidence at $\theta = 0^\circ$), the mutual orientation of the oscillating electric vector (which defines the direction of linear polarization) and the plane of incidence is not the same for each plane of incidence. Thus, in the following we consider (i) the component of the oscillating electric vector parallel to the (local) plane of incidence (local p polarization) and (ii) the component of the oscillating electric vector perpendicular to the local plane of incidence (local s polarization). Both arise as a result of the particular shape of the sample, while the global polarization of the light is determined by the experimental conditions.

From Eqs. (1)–(3), the (normalized) vector perpendicular to the local plane of incidence (local s polarization), along

$\vec{n} \times \vec{I}$, reads

$$\vec{s} = \frac{1}{\sin[i(\theta)]}\begin{pmatrix} -\sin\theta\cos I \\ \cos\theta\sin I \\ -\sin\theta\sin I \end{pmatrix}, \tag{6}$$

whereas the vector parallel to the plane of incidence (local p polarization) is along $\vec{I} \times \vec{s}$,

$$\vec{p} = \frac{1}{\sin[i(\theta)]}\begin{pmatrix} \cos\theta\sin I\cos I \\ \sin\theta \\ \cos\theta\sin^2 I \end{pmatrix}. \tag{7}$$

If the cylinder is illuminated by a globally P polarized light (we denote by uppercase letters the global polarizations and by lowercase letters the local ones), the corresponding electric vector decomposes on the local s and local p polarizations as

$$\vec{P} = \begin{pmatrix} \cos I \\ 0 \\ \sin I \end{pmatrix} = \frac{-\sin\theta\vec{s} + \cos\theta\sin I\,\vec{p}}{\sin[i(\theta)]}. \tag{8}$$

For an S-polarized light beam, one gets similarly

$$\vec{S} = \begin{pmatrix} 0 \\ 1 \\ 0 \end{pmatrix} = \frac{\cos\theta\sin I\vec{s} + \sin\theta\,\vec{p}}{\sin[i(\theta)]}. \tag{9}$$

As seen in Eq. (9), for a globally S polarized incident light, the oscillating electric field intensity vector is perpendicular to the plane of incidence only at the top of wire ($\theta = 0^\circ$). In turn, the polarization of rays contains both s and p components [Eq. (9)] for $\theta > 0^\circ$ and $\theta < 0^\circ$. The situation is qualitatively the same for globally P polarized light that conserves its p polarization at the top of the wire, $\theta = 0^\circ$ (and at the wire's edge, $\theta = 90^\circ$). The local polarization of globally p polarized light is neither p nor s as soon as θ differs from 0° (and 90°).

Once we parameterize the cylindrical geometry of the sample and local polarization of the incident light, we can proceed with the calculation of reflectivity. The general description of the magneto-optical properties in the physical-optics approximation is given by the Fresnel coefficients of reflection. In the first-order approximation of the magneto-optical effects and for a single air-magnetic-medium interface, the reflection coefficients for every combination of incident and reflected polarizations (s and p) are [28]

$$R_{ss} = \frac{\cos i - \hat{n}\cos t}{\hat{n}\cos t + \cos i}, \tag{10}$$

$$R_{sp} = \frac{-j\hat{Q}\sin(2i)\,m_l}{2\cos t(\hat{n}\cos t + \cos i)(\cos t + \hat{n}\cos i)}, \tag{11}$$

$$R_{pp} = \frac{\cos t - \hat{n}\cos i}{\cos t + \hat{n}\cos i} + \frac{j\hat{Q}\sin(2i)}{(\cos t + \hat{n}\cos i)^2}m_t, \tag{12}$$

$$R_{ps} = R_{sp}. \tag{13}$$

In these formulas, $\hat{n}$ is the complex index of refraction of the metal (divided by the index of oil/glass in case of immersion), i and t are the angles of incidence and transmission of the ray with respect to the interface normal (linked by the relation $\sin i = \hat{n}\sin t$, so that $\sin t$ and $\cos t$ are complex; note that we use $j^2 = -1$ to avoid ambiguities), m_l and m_t are the longitudinal and transverse components of surface magnetization (with respect to the plane of incidence), and $\hat{Q}$ is the complex Voigt magneto-optical parameter. The case of polar magnetization is treated separately at the end. In all calculations shown below, the optical parameters of iron at a wavelength of 550 nm were used: $\hat{n} = 2.95 - 2.93j$, and for the Voigt parameter we took $\hat{Q} = 0.042 - 0.119j$ [28].

B. Reflection from a nonmagnetic cylinder

In the first step, we consider a nonmagnetic cylinder, so that the Voigt parameter Q is zero and off-diagonal components R_{sp} and R_{ps} of the local reflection matrix $\overleftrightarrow{R}$ are zero as well. The amplitude of the light transmitted for an analyzer crossed by the polarizer is defined as a scalar product (for S-polarized incident light),

$$A_{SP} = \vec{P}\cdot(\overleftrightarrow{R}\,\vec{S}), \tag{14}$$

and vice versa for P-polarized incident light, where $\overleftrightarrow{R}$ denotes the reflection matrix which consists of Fresnel coefficients from Eqs. (10)–(13). The corresponding circumferential dependence of reflectivity for a crossed polarizer and analyzer is obtained from Eqs. (8), (9), and (14),

$$A_{PS} = A_{SP} = \frac{\sin\theta\cos\theta\,\sin \mathrm{I}}{\sin^2\theta + \cos^2\theta\sin^2 I}(R_{pp} - R_{ss}). \tag{15}$$

On the other hand, the reflectivity without the analyzer (and for S polarization of incident light) is obtained through

$$\overleftrightarrow{R}\vec{S} = \frac{\cos\theta\sin I\,R_{SS}\vec{s} + R_{PP}\sin\theta\,\vec{p}}{\sqrt{\sin^2\theta + \cos^2\theta\sin^2 I}}, \tag{16}$$

and hence the intensity is

$$I_S = |\overleftrightarrow{R}\vec{S}|^2 = \frac{|R_{pp}|^2\sin^2\theta + |R_{ss}|^2\cos^2\theta\sin^2 I}{\sin^2\theta + \cos^2\theta\sin^2 I}. \tag{17}$$

The circumferential dependences of reflectivity without analyzer and with a crossed polarizer and analyzer are compared in Figs. 5(a) and 5(b), respectively. The maximal reflectivity is achieved at the top of the cylinder (angle $\theta = 0^\circ$) for the case without an analyzer [Fig. 5(a)]. As seen, the reflectivity decreases progressively from the cylinder top on both sides and drops to zero at $\theta = 90^\circ$ and $\theta = -90^\circ$, where rays are no longer reflected.

The circumferential dependence of the reflectivity without an analyzer is qualitatively the same for any global incident angle I, and it has the same dependence for both S and P linear polarizations of the incident light.

However, if an analyzer crossed with a polarizer is inserted, the reflected light intensity profile changes drastically. As seen in Fig. 5(b), the profile consists of two maxima separated by a minimum at $\theta = 0^\circ$ in this case. The light intensity profile

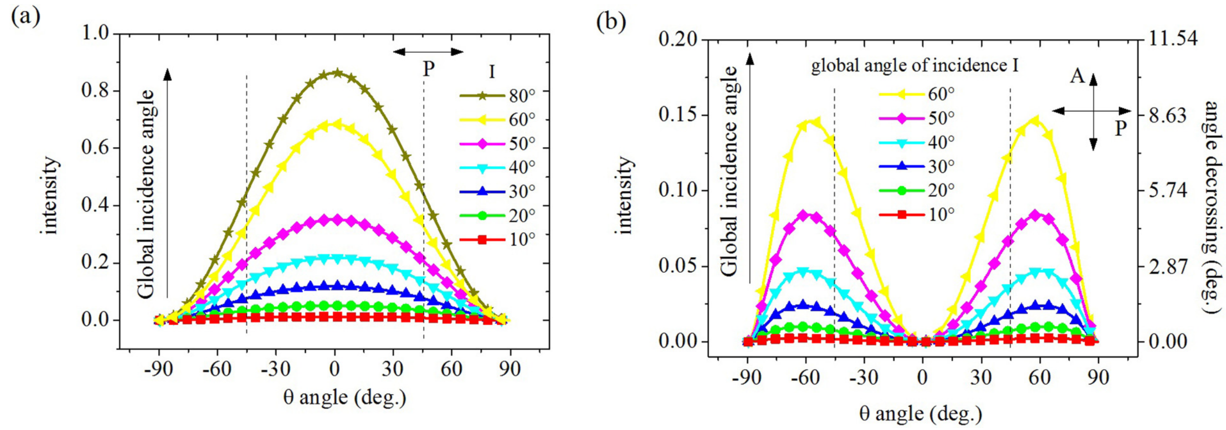

FIG. 5. (a) Calculated circumferential dependence of reflectivity for the nonmagnetic iron cylindrical surface without an analyzer and S-polarized incident light. (b) Light intensity transmitted through the crossed polarizer and analyzers when reflected from cylindrical surface. The right axis shows the corresponding decrossing angles. In both plots, dashed vertical lines depict the maximum angle ($\pm 45^{\circ}$) that can be observed with the microscope.

can be understood by the rotation of the plane of polarization when reflected from the cylindrical surface. As noted above, the polarization of each ray can be decomposed into two components of local polarizations with perpendicular and parallel orientation with respect to the local plane of incidence at $\theta > 0^{\circ}$ and $\theta < 0^{\circ}$. Since both of these components have different reflection coefficients [Eqs. (10) and (13)], the polarization direction changes with reflection. Such rotation of light polarization is not related to the interaction with surface magnetization (like MOKE) but stems purely from the composite nature of local polarization. The effect of mixed p and s polarization on resulting magneto-optical contrast was previously observed in diffracted beams from a periodic array of thin deposited disks [29] and plasmonic crystals [30]. However, in the case of magnetic cylinders, such an effect stems from the curved topography of cylindrical samples. As seen in Fig. 5(b), the equivalent value of the polarization rotation is much bigger ($2^{\circ}-8^{\circ}$) than typical values of Kerr rotation, obscuring the magnetic contrast. Thus, the cylindrical shape of the sample is an important factor that must be taken into account to interpret magneto-optical observations. As seen in Fig. 5, the relative change in reflectivity increases remarkably with the global angle of incidence, but the angular position of the maxima is more or less the same ($\theta = \pm 62^{\circ}$, beyond the observable range).

This analytical calculation of the circumferential dependence of reflectivity is confirmed qualitatively by optical observations of $Fe_{77.5}Si_{7.5}B_{15}$ microwires. Figure 6 shows that reflection of linearly polarized light without an analyzer gives a single intensity maximum, while two intensity maxima (two bright stripes) appear with a crossed polarizer and analyzer, similar to the plot in Fig. 5. Since the highest

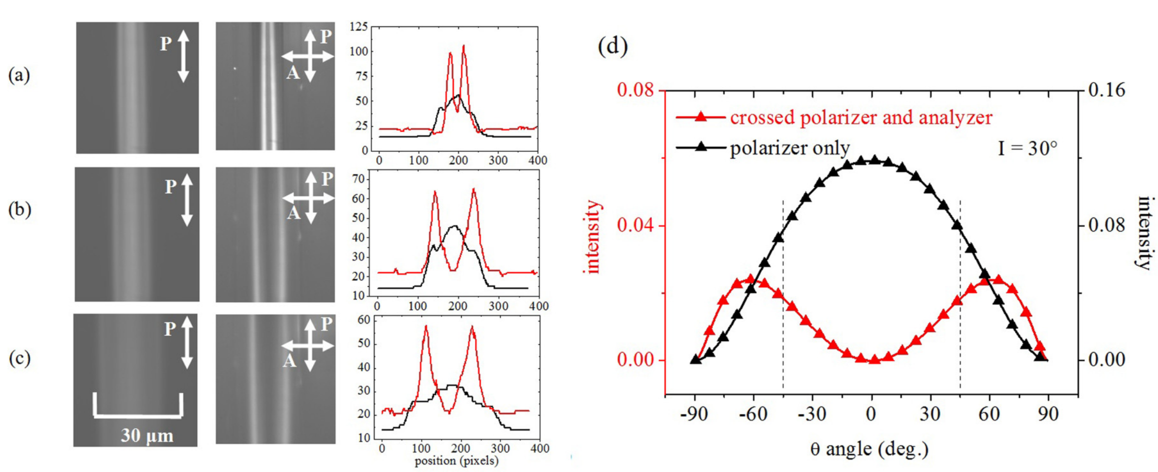

FIG. 6. The intensity profile of light reflected from cylindrical surface of $Fe_{77.5}Si_{7.5}B_{15}$ amorphous glass-coated microwire for different focusing depths of (a) 2, (b) 3, and (c) 4 μm below the top surface of the metallic nucleus. The left column shows the optical image of microwires observed by P-polarized light, whereas the right column compares the images obtained with a crossed polarizer and analyzer. Graphs on the right show the corresponding profiles when observed with a polarizer (black curve) and with a crossed polarizer and analyzer (red curve). The scale of light intensity is very different between both cases. As seen in the left and right columns, the presence of two cylindrical surfaces (glass coat and metallic core) results in two superimposed profiles from Fig. 5(a). All images are taken using immersion oil. (d) Theoretical calculation of intensity for both cases (i) with a polarizer and analyzer and (ii) for only a polarizer.

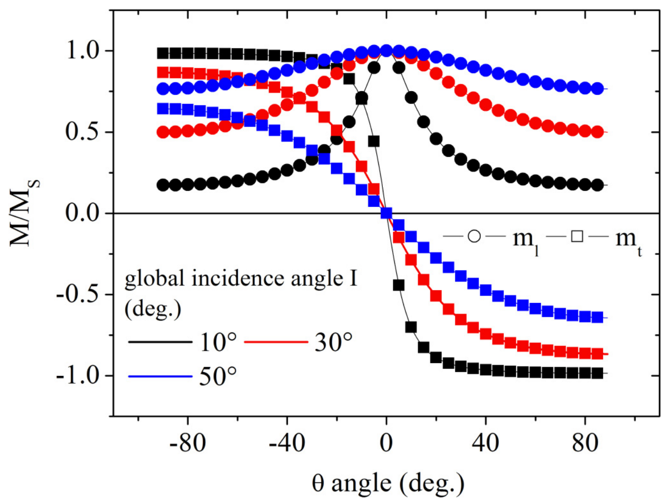

FIG. 7. Components of the local magnetization with respect to the local plane of incidence: longitudinal (m_l) and transverse (m_t) for an axially magnetized cylinder. For a circularly magnetized cylinder, these components are simply exchanged. Dashed vertical lines depict the maximum angle ($\pm 45^\circ$) that can be observed with the microscope.

intensity of reflected light without an analyzer is obtained at the top of the wire (Fig. 6), the two light stripes observed with crossed polarizer and analyzer (Fig. 6) cannot result from imperfections of polarizers. The increasing separation of the two stripes when focusing below the top surface is qualitatively expected (points of the wire surface that come into focus). For a quantitative comparison, a full calculation of the microscope image would be required.

C. Reflection from a magnetic cylinder

A calculation of the magneto-optical contrast for all orientations of incident light (including various polarizations) and the direction of surface magnetization is beyond the scope of this work. Here, we confine our calculation to three limiting configurations: (i) spontaneous magnetization along the main axis, (ii) circular surface magnetization, and (iii) polar surface magnetization.

1. Axially magnetized cylinder

For an axially magnetized cylinder, the local magnetization components (i.e., with respect to the local planes of incidence) to be inserted in Eqs. (11) and (12) read, from Eqs. (6) and (7),

$$m_t = \vec{m} \cdot \vec{s} = -\sin\theta \cos I / \sin[i(\theta)],$$
$$m_l = \vec{m} \cdot (\vec{s} \times \vec{n}) = \sin I / \sin[i(\theta)], \quad (18)$$

with the polar component being zero. These formulas show that, even if the surface magnetization is along the global longitudinal direction, in the local plane of incidence it has a transverse component m_t that is odd in the angle θ [8] (Fig. 7).

The reflectivities are given by the Fresnel coefficients, Eqs. (10)–(13) as before, but a nonzero Voigt constant must be taken. Then, the off-diagonal components R_{sp} (and R_{ps}) of the reflection matrix $\overleftrightarrow{R}$ are not zero, and the circumferential dependence of the light intensity after the crossed polarizer and analyzer (along the principal directions S and P) can be evaluated from

$$A_{SP} = A_{PS} = \vec{P} \cdot (\overleftrightarrow{R}\,\vec{S}) = \frac{\sin\theta \cos\theta \sin I\,(R_{pp} - R_{ss}) + (\cos^2\theta \sin^2 I - \sin^2\theta) R_{sp}}{\sin^2\theta + \cos^2\theta \sin^2 I}. \quad (19)$$

Plots of the intensity computed from Eq. (19) for both axial directions of surface magnetization, $+\vec{M}_S$ and $-\vec{M}_S$, are compared in Fig. 8(a). As seen, due to the small value of Q, the interaction of light with surface magnetization results in very small changes in light intensity.

Our extended MOKE microscopy setup utilizes a differential imaging technique, in which the magnetic contrast is visualized by subtraction of a background image (for example, the sample before reversal) from the image of the sample after reversal. The magnetic contrast corresponding to the axial change in surface magnetization from $+\vec{M}_S$ to $-\vec{M}_S$ is then given by

$$\Delta I_{SP} = |A_{SP}(+M_S)|^2 - |A_{SP}(-M_S)|^2. \quad (20)$$

A plot of Eq. (20) is shown in Fig. 8(b). As seen, the axial change in surface magnetization results in the appearance of a black and white magneto-optic contrast that is largest for $I = 70^\circ$. In the visible range, the contrast grows with both θ and I.

These calculations can be compared to the observations of the surface reversal process invoked by axial domain wall propagation in a $Fe_{77.5}Si_{7.5}B_{15}$ microwire. Such a composition is characterized by a very thin shell of surface domains (<10 nm) due to the high magnetostriction of the alloy [14]. Alternatively, the absence of the surface shell of the domain would allow observation of the axial domain directly, which could explain the black-and-white contrast observed in the experiment [Fig. 9(a)]. Note that a small uncrossing of the polarizer and analyzer leads to asymmetry in the heights of intensity maxima ($\pm 2\%$ of the crossed intensity for a 1° decrossing).

As seen in Fig. 9, the axial change in the magnetization results in the black-and-white contrast, in agreement with the model. Interestingly, such magnetic contrast is independent of the direction of incident light (i.e., $+I$ or $-I$) [8], which can be understood by the formulas given. Moreover, the magnetic contrast appears to be determined by the sample shape rather than by the configuration of the microscope (normal incident light for the polar Kerr effect and inclined light for

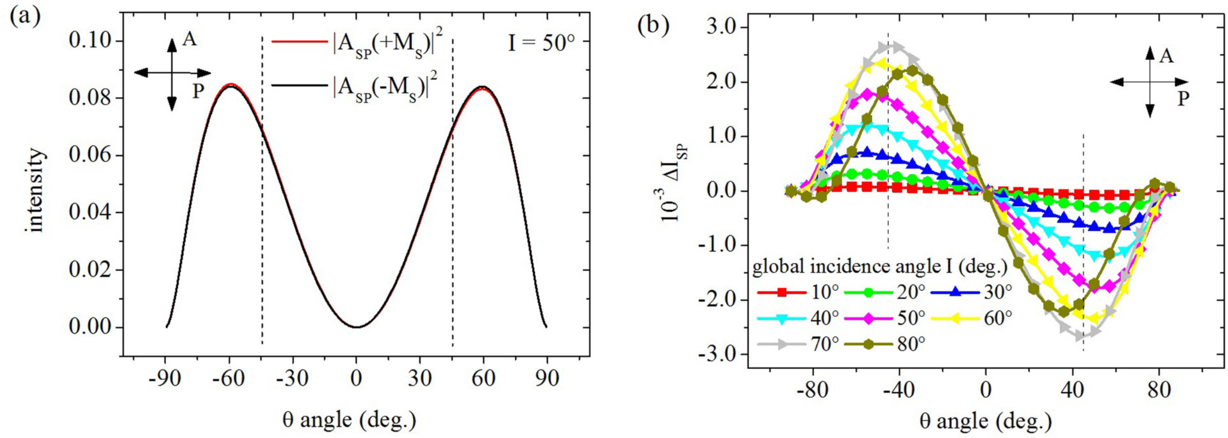

FIG. 8. (a) Calculation of the intensity profile of light reflected from a cylinder magnetized axially. (b) Change in the light intensity profile that occurs by reversal of surface axial magnetization. In both plots, dashed vertical lines depict the maximum angle (±45°) that can be observed with the microscope.

the longitudinal Kerr effect with respect to the wire axis), which confirms the important role of cylindrical geometry on magneto-optical observations. We note that similar contrasts were reported recently in another study [20,22].

As seen in Fig. 10, both longitudinal and transverse components of the local magnetization contribute to a magnetic contrast that is odd with angle θ. The longitudinal component prevails for small values of angle θ. At higher angles, when the effect of the longitudinal component changes its sign, it is overcome by the transverse component with the same polarity as the longitudinal one for small angles. Thus, their sum results in uniform (and opposite) magnetic contrast for each side of the cylinder. At small angles θ, the contrast is close to linear [compare to Fig. 9(b)].

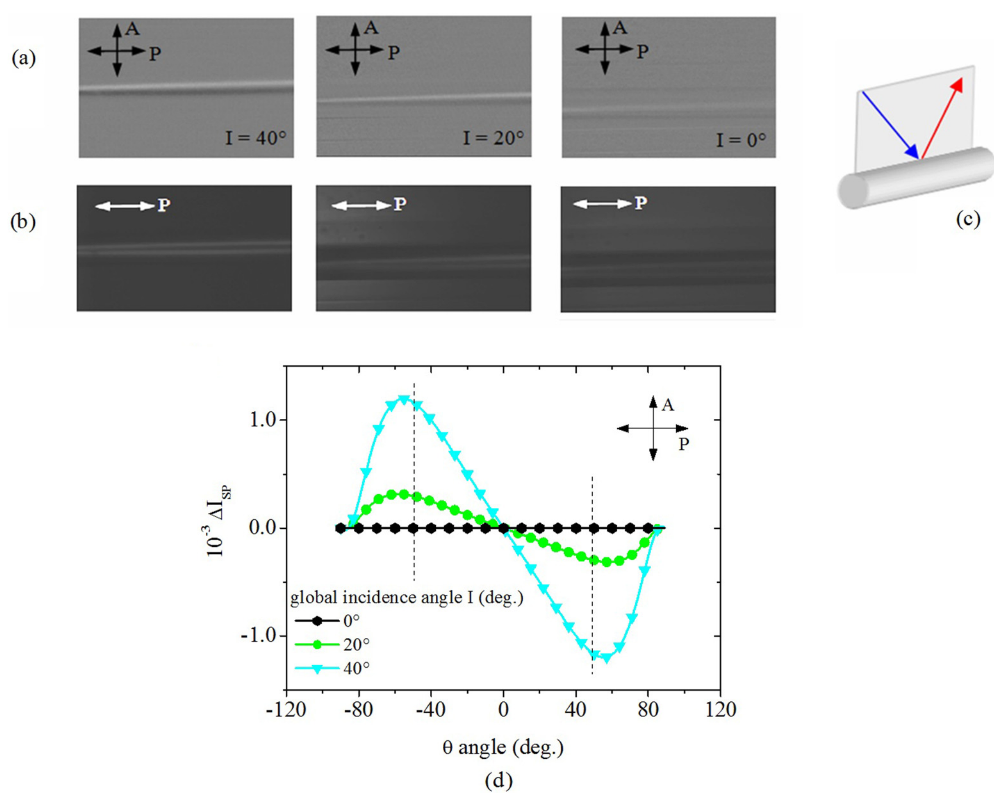

FIG. 9. (a) Magneto-optical contrast for an axial magnetization change in a $Fe_{77.5}Si_{7.5}B_{15}$ microwire for various global angles of incidence. (b) Light intensity for a positive axial magnetization $+M_S$. (c) Scheme of the observations by illumination of the wire along its main axis, with P polarization. Note that magneto-optical contrast decreases with the global angle of incidence, in agreement with calculation in Fig. 8(b). (d) Calculation of magneto-optical contrast for an axially magnetized cylinder and for a crossed polarizer and analyzer.

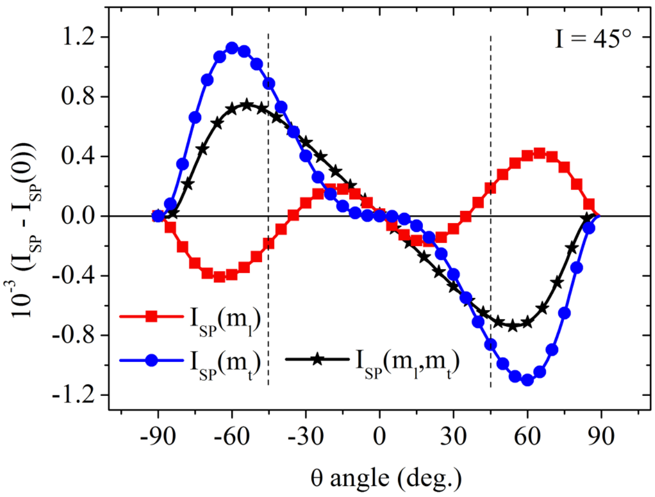

FIG. 10. Two contributions to the overall magnetic contrast (black curve) for the axially magnetized cylinder (change in I_{SP} compared to the nonmagnetic case). The contribution of the local magnetization longitudinal (transverse) is marked in red (blue). Dashed vertical lines depict the maximum angle ($\pm 45^{\circ}$) that can be observed with the microscope.

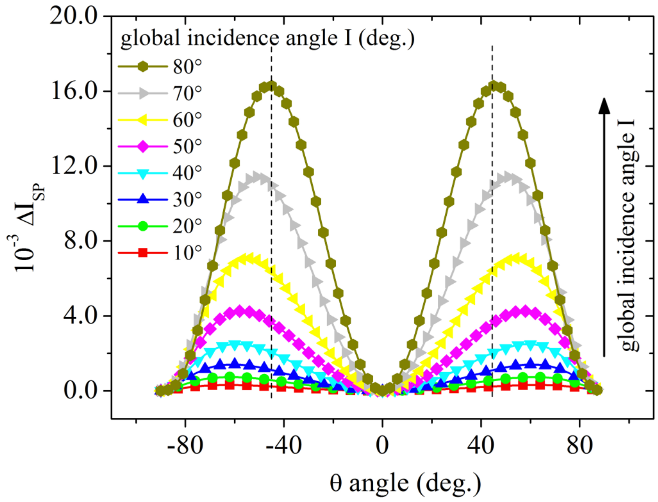

FIG. 11. Calculated change in the light intensity profile that occurs by reversal of surface circular magnetization for a crossed polarizer and analyzer (along the principal S and P directions). Dashed vertical lines depict the maximum angle ($\pm 45^{\circ}$) that can be observed with the microscope.

2. Circularly magnetized cylinder

For this case, we consider a surface magnetization that lies in the yz plane and hence a local magnetization reading

$$\vec{m} = \begin{pmatrix} 0 \\ \cos\theta \\ -\sin\theta \end{pmatrix}. \tag{21}$$

The components of the local magnetization with respect to the local plane of incidence are, from Eqs. (1) and (6),

$$\begin{aligned} m_t &= \vec{m}\cdot\vec{s} = \sin I/\sin[i(\theta)], \\ m_l &= \vec{m}\cdot(\vec{s}\times\vec{n}) = \cos I\,\sin\theta/\sin[i(\theta)]. \end{aligned} \tag{22}$$

Making a comparison to the axial case, Eq.(18), one sees that the longitudinal and transverse components are simply exchanged, so that the longitudinal component m_l is now an odd function of the angle θ. Note that, as magnetization is tangent to the surface, the local polar component is still zero.

Inserting Eq. (22) into Eq. (19) and calculating the change in the light intensity for both circulations of surface magnetization, Eq. (20), one gets the light intensity profile plotted in Fig. 11.

Contrary to the axial change in surface magnetization, the circular one gives a magneto-optical contrast consisting of two light stripes of the same polarity. Such a light intensity profile can be understood by a dominant contribution of the local transverse magnetization m_t that is an even function of the angle θ (Fig. 7). We note also that the contrast is about 5 times larger than in the axial case. With uncrossing the polarizer and analyzer by a small angle, the magneto-optical contrast remains qualitatively the same.

As seen in Fig. 12, the longitudinal component of local magnetization gives a negative contrast for small values of the angle θ; however, it is always overcome by the magnetic contrast coming from the local transverse magnetization.

3. Cylinder with polar magnetization

For surface magnetization spontaneously oriented in polar direction, we write

$$\vec{m} = \begin{pmatrix} 0 \\ \sin\theta \\ \cos\theta \end{pmatrix} \tag{23}$$

In this case, the polar component $\vec{m}_p = \vec{n},\vec{m}$ is one, in-plane components of local magnetization zero, $m_t = m_l = 0$, and corresponding Fresnel coefficients $R^{\perp}$ for polar magnetization

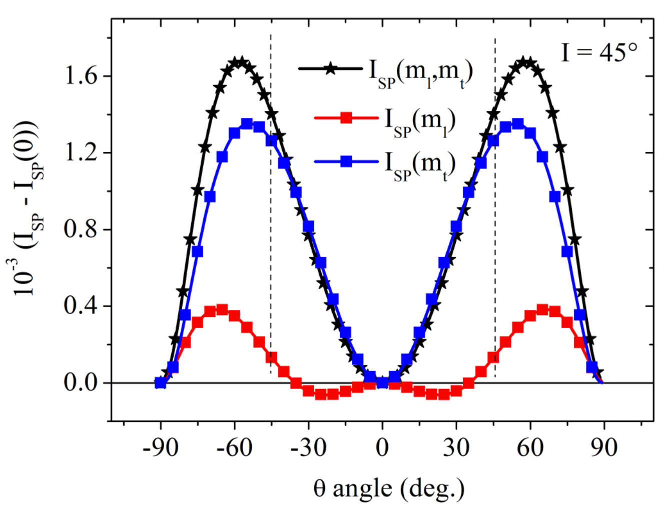

FIG. 12. Calculation of the two contributions to the overall magnetic contrast for a circularly magnetized cylinder. The calculation is obtained from Eqs. (22) and (10)–(14). Dashed vertical lines depict the maximum angle ($\pm 45^{\circ}$) that can be observed with the microscope.

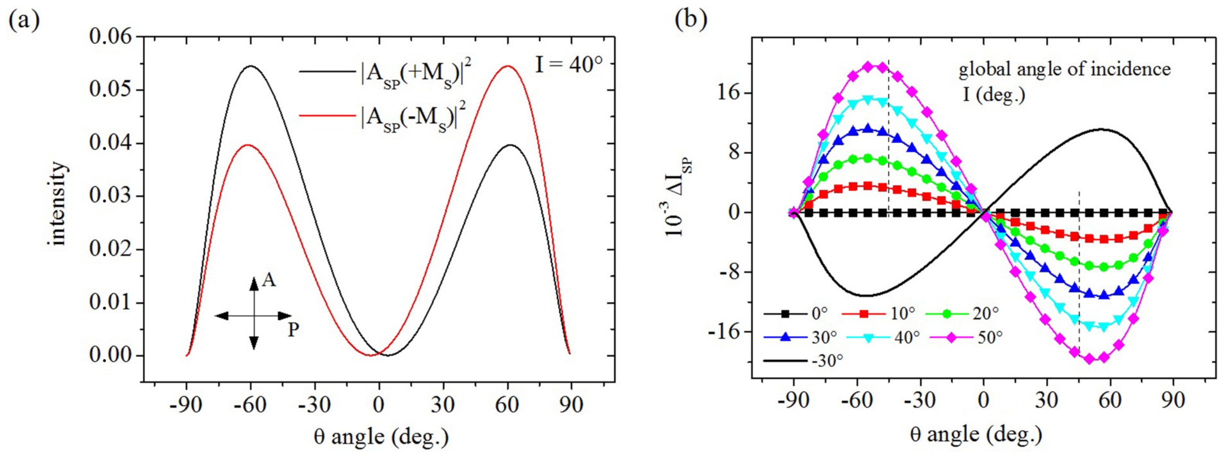

FIG. 13. (a) Calculation of the intensity profile of light reflected from a cylinder magnetized in the polar direction. (b) Change in the light intensity profile that occurs by reversal of surface polar magnetization. In both plots, dashed vertical lines depict the maximum angle (±45°) that can be observed with the microscope.

m_p can be read from [28] as

$$R_{ss}^{\perp} = R_{ss}, \tag{24}$$

$$R_{pp}^{\perp} = R_{pp}, \tag{25}$$

$$R_{sp}^{\perp} = \frac{\hat{j}\,\hat{Q}\hat{n}\cos i\, m_p}{(\hat{n}\cos i + \mathrm{cos} t)(\hat{n}\cos t + \cos i)}, \tag{26}$$

$$R_{ps}^{\perp} = -R_{sp}^{\perp}. \tag{27}$$

The light intensity profile for polar magnetization can be obtained by inserting Fresnel coefficients (24)–(27) into (19) [generalized for $R_{sp} \neq R_{ps}$] and utilizing (23). Figure 13 shows that a change in the polar magnetization generates black-and-white contrast, similar to the case of axial magnetization.

For polar magnetization, the amplitude of the contrast reaches up to 20×10^{-3}, which is approximately 8 times bigger than the contrast generated by axial magnetization [Fig. 8(b)]. The simplest way to distinguish between axial and polar surface magnetizations is to compare the resulting magneto-optical contrast for two opposite global angles of incidence. Figure 13(b) shows that by reversing the global angle of incidence, the polarity of black-and-white contrast is reversed too [see $I = \pm 30^{\circ}$ in Fig. 13(b)] in the case of polar magnetization. On the other hand, the polarity of black-and-white contrast does not depend on the sign of the global angle of incidence for the axial change in the surface magnetization [Fig. 8(b)]. The magneto-optical contrast of the same polarity for both opposite global angles of incidence was observed in FeSiB previously [8], which implies that surface magnetization has an axial direction.

The black-and-white contrast is sometimes attributed to a helical surface domain structure that is reversed by internal domain wall propagation in the inner core of the wire [31]. However, our experiments with a domain wall trapped in a potential well [8] show that even if the wall has opposite tilting [Figs. 14(a) and 14(b)], the magneto-optical contrast remains the same. This contradicts the helical structure hypothesis, according to which domain walls at the surface should have a tilt fixed by the helix.

IV. CONCLUSIONS

We have presented a comprehensive analysis of the magneto-optical observations of ferromagnetic cylinders. This framework will obviously not apply to nanowires that are subwavelength in diameter, for which diffraction effects appear. On the other hand, for large-diameter wires, it will become appropriate to consider only the tangent plane at the top of the wire's surface. For the intermediate regime, we have shown that the curvature of the cylindrical surface gives rise to a circumferential dependence of reflectivity due to variations in the angle of incidence, numerical aperture, and spatial orientation of planes of incidence. When the cylinder is illuminated along its main axis by linearly polarized light, the axial change in surface magnetization results in the appearance of a black-and-white contrast. This study shows the complexity of the optical magnetic imaging of microwires, whose radius is not very large compared to the wavelength of light. It is a first step towards a full calculation of magneto-optical microscope images in such samples.

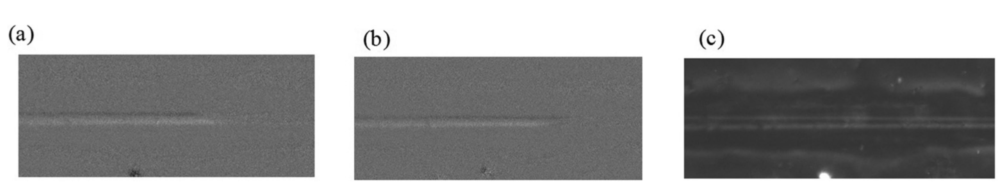

FIG. 14. (a) and (b) Magneto-optical images of the domain wall in FeSiB microwire. (c) Corresponding optical image.

ACKNOWLEDGMENTS

This work was partially supported by the RTRA Triangle de la Physique (IMAPLAN project) and by the Slovak projects APVV-16-0079, VEGA No. 1/0164/16, and VVGS-2016-320. K.R. benefited from a Bourse du gouvernement français.

[1] A. Fernández-Pacheco, L. Serrano-Ramón, J. M. Michalik, M. R. Ibarra, J. M. De Teresa, L. O'Brien, D. Petit, J. Lee, and R. P. Cowburn, Three dimensional magnetic nanowires grown by focused electron-beam induced deposition, Sci. Rep. **3**, 1492 (2013).

[2] L. O'Brien, D. E. Read, H. T. Zeng, E. R. Lewis, D. Petit, and R. P. Cowburn, Bidirectional magnetic nanowire shift register, Appl. Phys. Lett. **95**, 232502 (2009).

[3] K.-J. Kim, J.-Ch. Lee, S.-J. Yun, G.-H. Gim, K.-S. Lee, S.-B. Choe, and K.-H. Shin, Electric control of multiple domain walls in Pt/Co/Pt nanotracks with perpendicular magnetic anisotropy, Appl. Phys. Express **3**, 083001 (2010).

[4] O. Idigoras, E. Nikulina, J. M. Porro, P. Vavassori, A. Chuvilin, and A. Berger, FEBID fabrication and magnetic characterization of individual nano-scale and micro-scale Co structures, Nanofabrication **1**, 23 (2014).

[5] W. Jiang, P. Upadhyaya, W. Zhang, G. Yu, M. B. Jungfleisch, F. Y. Fradin, J. E. Pearson, Y. Tserkovnyak, K. L. Wang, O. Heinonen, S. G. E. te Velthuis, and A. Hoffmann, Blowing magnetic skyrmions bubbles, Science **349**, 283 (2015).

[6] Y. Gao, B. You, X. Z. Ruan, M. Y. Liu, H. L. Yang, Q. F. Zhan, Z. Li, N. Lei, W. S. Zhao, D. F. Pan, J. G. Wan, J. Wu, H. Q. Tu, J. Wang, W. Zhang, Y. B. Xu, and J. Du, Depinning of domain walls in permalloy nanowires with asymmetric notches, Sci. Rep. **6**, 32617 (2016).

[7] A. Stupakiewicz, A. Chizhik, M. Tekielak, A. Zhukov, J. Gonzalez, and A. Maziewski, Direct imaging of the magnetization reversal in microwires using all-MOKE microscopy, Rev. Sci. Instrum. **85**, 103702 (2014).

[8] K. Richter, A. Thiaville, and R. Varga, Magneto-optical study of the surface reversal process in amorphous glass-coated microwires with positive magnetostriction, IEEE Trans. Magn. **50**, 2501404 (2014).

[9] M. Yan, A. Kákay, S. Gliga, and R. Hertel, Beating the Walker Limit with Massless Domain Walls in Cylindrical Nanowires, Phys. Rev. Lett. **104**, 057201 (2010).

[10] R. Varga, A. Zhukov, V. Zhukova, J. M. Blanco, and J. Gonzalez, Supersonic domain wall in magnetic microwires, Phys. Rev. B **76**, 132406 (2007).

[11] K. Chichay, V. Zhukova, V. Rodionova, M. Ipatov, A. Talaat, J. M. Blanco, J. Gonzalez, and A. Zhukov, Tailoring of domain wall dynamics in amorphous microwires by annealing, J. Appl. Phys. **113**, 17A318 (2013).

[12] V. Zhukova, V. S. Larin, and A. P. Zhukov, Stress induced magnetic anisotropy and giant magnetoimpedance in Fe-rich glass-coated magnetic microwires, J. Appl. Phys. **94**, 1115 (2003).

[13] A. Zhukov, J. M. Blanco, M. Ipatov, A. Chizhik, and V. Zhukova, Manipulation of domain wall dynamics in amorphous microwires through the magnetoelastic anisotropy, Nanoscale Res. Lett. **7**, 223 (2012).

[14] J. Olivera, M. L. Sanchez, V. M. Prida, R. Varga, V. Zhukova, A. P. Zhukov, and B. Hernando, Temperature dependence of the magnetization reversal process and domain structure in FeNiSiB magnetic microwires, IEEE Trans. Magn. **44**, 3946 (2008).

[15] V. Rodionova, A. Nikoshin, J. Torrejon, G. A. Badini-Confalonieri, N. Perov, and M. Vazquez, Temperature-dependent magnetic properties of magnetically biphase microwires, IEEE Trans. Magn. **47**, 3787 (2011).

[16] K. Richter, R. Varga, G. A. Badini-Confalonieri, and M. Vázquez, The effect of transverse field on fast domain wall dynamics in magnetic microwires, Appl. Phys. Lett. **96**, 182507 (2010).

[17] R. M. A. Azzam and N. M. Bashara, Polarization characteristics of scattered radiation from a diffraction grating by ellipsometry with application to surface roughness, Phys. Rev. B **5**, 4721 (1971).

[18] A. Chizhik, R. Varga, A. Zhukov, J. Gonzalez, and J. M. Blanco, Kerr-effect based Sixtus-Tonks experiment for measuring the single domain wall dynamics, J. Appl. Phys. **103**, 07E707 (2008).

[19] E. E. Shalygina, V. V. Molokanov, and M. A. Komarova, Magnetooptical investigation of the micromagnetic structure and magnetization processes in $Co_{69}Fe_4Si_{12}B_{15}$ amorphous microwires, J. Exp. Theor. Phys. **95**, 511 (2002).

[20] A. Chizhik, A. Stupakiewicicz, A. Zhukov, A. Maziewski, and J. Gonzales, Experimental demonstration of basic mechanisms of magnetization reversal in magnetic microwires, Phys. B (Amsterdam, Neth.) **435**, 125 (2014).

[21] H. Chiriac, T.-A. Óvári, and M. Tibu, Effect of surface domain structure on wall mobility in amorphous microwires, J. Appl. Phys. **105**, 07A310 (2009).

[22] R. Schäfer, Investigation of domains and dynamics of domain walls by the magneto-optical Kerr effect, in *Handbook of Magnetism and Advanced Magnetic Materials*, edited by H. Kronmüller and S. Parkin (John Wiley & Sons, Ltd., Hoboken, NJ, USA, 2007), Vol. 3, p. 1513.

[23] G. F. Taylor, A method of drawing metallic filaments and a discussion of their properties and uses, Phys. Rev. **23**, 655 (1924).

[24] M. Vazquez and A. P. Zhukov, Magnetic properties of glass-coated amorphous and nanocrystalline microwires, J. Magn. Magn. Mater. **160**, 223 (1996).

[25] G. S. Krinchik and V. A. Artemjev, Magneto-optic properties of nickel, iron, and cobalt, J. Appl. Phys. **39**, 1276 (1968).

[26] K. Richter, R. Varga, and A. Zhukov, Influence of thermal treatment on domain wall dynamics in glass-coated microwires, Acta Phys. Pol. A **118**, 738 (2010).

[27] P. Beckmann and A. Spizzichino, *The Scattering of Electromagnetic Waves from Rough Surfaces* (Pergamon, Oxford, 1963), Chaps. 3 and 8.

[28] G. Träger, L. Wenzel, and A. Hubert, Computer experiments on the information depth and the figure of merit in magnetooptics, Phys. Status Solidi A **131**, 201 (1992).

[29] T. Verduci, C. Rufo, A. Berger, V. Metlushko, B. Ilic, and P. Vavassori, Fourier magnetic imaging, Appl. Phys. Lett. **99**, 092501 (2011).
[30] C. Billaudeau, S. Collin, Ch. Sauvan, N. Bardou, F. Pardo, and J.-L. Pelouard, Angle-resolved transmission measurements through anisotropic two-dimensional plasmonic crystals, Opt. Lett. **33**, 165 (2008).
[31] A. Chizhik, A. Zhukov, J. Gonzalez, and A. Stupakiewicz, Control of the domain wall motion in cylindrical magnetic wires, Appl. Phys. Lett. **109**, 052405 (2016).